The entrance pupil of the human eye

Geoffrey K Aguirre

Department of Neurology
University of Pennsylvania, Philadelphia, PA, USA

The pupil aperture of the iris is subject to refraction by the cornea, and thus an outside observer sees a virtual image: the "entrance pupil" of the eye. When viewed off-axis, the entrance pupil has an elliptical form. The precise appearance of the entrance pupil is the consequence of the anatomical and optical properties of the eye, and the relative positions of the eye and the observer. This paper presents a ray-traced, exact model eye that provides the parameters of the entrance pupil ellipse for an observer at an arbitrary location and for an eye that has undergone biologically accurate rotation. The model is able to reproduce empirical measurements of the shape of the entrance pupil with good accuracy. I demonstrate that accurate specification of the entrance pupil of a stationary eye requires modeling of: corneal refraction, the misalignment of the visual and optical axes, the thickness of the iris, and the non-circularity of the pupil aperture. The model specifies the location of the fovea in the posterior chamber, and this location varies for eyes modeled with different spherical refractive error. The resulting dependency of the visual axis upon ametropia agrees with prior empirical measurements. The model, including a three-dimensional ray-tracing function through ellipsoidal surfaces, is implemented in open-source MATLAB code.

Keywords: pupil

Introduction

The pupil is the aperture stop of the optical system of the eye. When viewed from the outside, an observer sees the *entrance* pupil of the eye, which is the image of the pupil as seen through corneal refraction. The precise appearance of the entrance pupil depends upon the anatomical and optical properties of the eye, as well as the relative positions of the eye and the observer. Characterization of the entrance pupil is relevant for modeling the off-axis image-forming properties of the eye (Bradly & Thibos, 1995), optimizing corneal surgery (Uozato & Guyton, 1987), and performing model-based eye-tracking (Barsingerhorn et al., 2017).

The appearance of the entrance pupil as a function of horizontal viewing angle has been the subject of empirical measurement over some decades (Spring & Stiles, 1948; Jay, 1962). As an observer views the eye from an increasingly oblique angle, the pupil takes on an ever-more ellipitical appearance. Mathur et al. (2013) measured the shape of the entrance pupil as a function of the nasal and temporal visual field position of a camera moved about a stationary eye. The ratio of the minor to major axis length of the pupil ellipse (essentially the horizontal-to-vertical aspect ratio) was well fit by a decentered and flattened cosine function of viewing angle. Fedtke et al. (2010) obtained a function with similar form by ray trace simulation of the Navarro et al. (1985) model eye. This work did not address the appearance of the entrance pupil for the circumstance of a stationary camera and a rotating eye.

Here I present a ray-traced model eye that provides the ellipse parameters of the entrance pupil as seen by an observer at an arbitrary location. The model accounts for individual variation in spherical refractive error. The location of the fovea is specified and used to derive separate visual and optical axes; the angle between them (α) varies as a function of ametropia. The open-source MATLAB code (`https://github.com/gkaguirrelab/gkaModelEye`) implements a light-weight, invertible ray-tracing solution that can incorporate artificial lenses (e.g., spectacles, contacts) in the optical path between eye and observer. I demonstrate that the measurements

doi: Received: May 17, 2018 ISSN 1534–7362 © 20?? ARVO

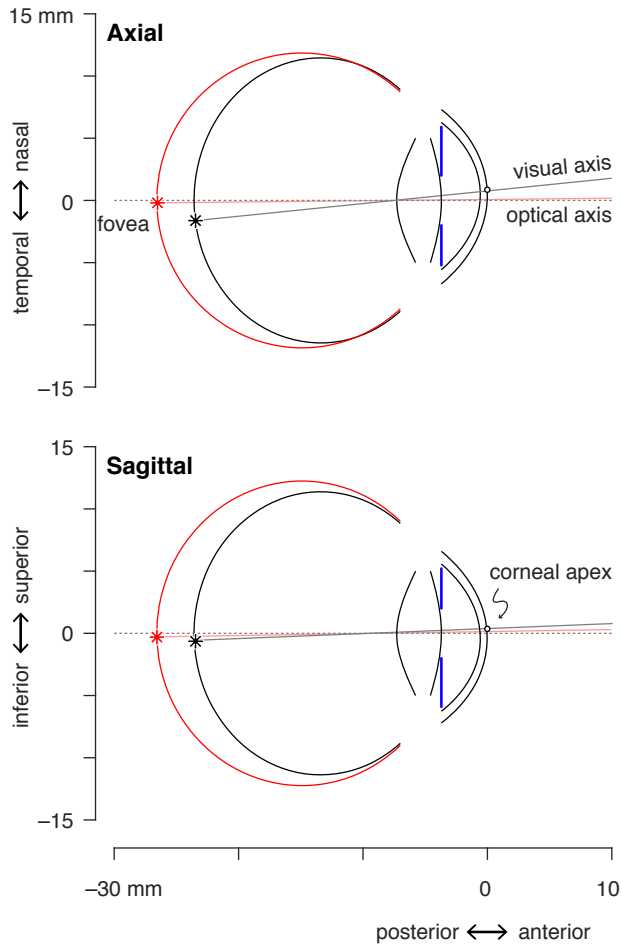

Figure 1: **Schematic of the model eye** The components of the model are shown for two right eyes with differing spherical refractive errors. In black is the model of an emmetropic eye, and in red that of an eye with a –10 refractive error. The myopic eye has a larger, and more spherical, posterior chamber. The model specifies the location of the fovea (asterisk), and in the model myopia brings the fovea closer to the posterior apex of the posterior chamber. Consequently the visual axis (solid line) moves to closer alignment with the optical axis (dotted line). There is a difference in the curvature of the front corneal surface between the emmetropic and myopic eyes, but this is too small to be seen in the illustration.

of Mathur et al. (2013) can be replicated with good accuracy if the model incorporates *i*) corneal refraction, *ii*) the separation of the visual and optical axes, *iii*) the thickness of the iris, and *iv*) the non-circularity and tilt of the aperture stop. The behavior of the model across changes in spherical ametropia, including changes in the location of the visual axis of the eye, compares favorably to empirical results. Finally, I equip the model with biologically accurate rotation centers, and examine the appearance of the entrance pupil in a moving eye.

Model eye

The properties of the model are specified in software. The coordinate system is based on the optical axis, with the dimensions corresponding to axial, horizontal, and vertical position. The optical and pupillary axes are equivalent. Units are given in mm and degrees, with the exception of the tilt component of the ellipse parameters, which is specified in radians. Axial depth is given relative to the anterior-most point of the front surface of the cornea, which is assigned a depth position of zero. Parameters are presented for a right eye. An axial and sagittal schematic of the model eye is presented in Figure 1.

Anatomical components

Cornea

The front surface of the cornea is modeled as a tri-axial ellipsoid, taking the "canonical representation" from Navarro et al. (2006) for the emmetropic eye. Atchison (2006) observed that the radius of curvature at the vertex of the cornea varies as a function of spherical ametropia, and provided the parameters for a rotationally-symmetric, prolate ellipsoid, with the radius of curvature (but not asphericity) varying linearly with the refractive error of the modeled eye. I calculated the proportional change in the Navarro values that would correspond to the effect modeled by Atchison (2006). This yields the following expression for the radii of the corneal front surface ellipsoid:

$$cornea_front_radii(SR) = \begin{bmatrix} 14.26 & 10.43 & 10.27 \end{bmatrix} \cdot (1 - 0.0028SR) \tag{1}$$

where SR is spherical refractive error in diopters, and the radii are given in the order of $\begin{bmatrix} axial & horizontal & vertical \end{bmatrix}$.

Atchison (2006) finds that the back surface of the cornea does not vary by ametropia. Navarro et al. (2006) does not provide posterior cornea parameters. Therefore, I scale the parameters provided by Atchison (2006) to be proportional to the axial corneal radius specified by Navarro:

$$cornea_back_radii = \begin{bmatrix} 13.7716 & 9.3027 & 9.3027 \end{bmatrix} \tag{2}$$

The center of the back cornea ellipsoid is positioned so that there is 0.55 mm of corneal thickness between the front and back surface of the cornea at the apex, following Atchison (2006).

Navarro et al. (2006) measured the angle of rotation of the axes of the corneal ellipsoid relative to the keratometric axis (the axis that connects a fixation point with the center of curvature of the cornea). Here, I convert these angles to be relative to the optic axis of the eye. To do so, I make the approximation that the keratometric axis is equal to the fixation axis, and then add the Navarro measurements to the angle between the visual and optical axes for the emmetropic eye (described below). The final parameters (–3.45, 1.44, –0.02, degrees azimuth, elevation, and torsion) describe a corneal ellipsoid that is tilted so that the corneal apex is directed towards the superior, nasal field.

Iris and pupil

The iris is modeled as a thin cylinder perpendicular to the optical axis (i.e., zero "iris angle"), with the anterior surface positioned at a depth equal to the anterior point of the lens. For the simulations conducted here, I assumed a cycloplegic eye to match the Mathur et al. (2013) experimental conditions, and thus the anterior surface of the iris was positioned 3.9 mm posterior to the anterior surface of the cornea (Drexler et al., 1997). The pupil is an aperture in the iris, centered on the optical axis. Because the iris has a non-zero thickness, there is a front and back pupil aperture. While the measured thickness of the iris close to the scleral spur is ∼0.4 mm (He et al., 2009), the iris is thinner and has a rounded edge at the pupil border. The model assigns an iris thickness of 0.15 mm at the pupil aperture.

The pupil aperture is modeled as slightly non-circular. Wyatt (1995) measured the average (across subject) ellipse parameters for the entrance pupil under dim and bright light conditions (with the visual axis aligned with camera axis). The pupil was found to be elliptical in both circumstances, with a horizontal long axis in bright light, and a vertical long axis in dim light. The elliptical eccentricity was less for the constricted as compared to the dilated pupil (non-linear eccentricity ϵ = 0.12 horizontal; 0.21 vertical). In the current model, I limit the eccentricity of the dilated entrance pupil to a slightly lower value (0.18) to provide a better fit to the measurements of Mathur et al. (2013) (discussed below). Accounting for the refraction of the cornea, I calculated the ellipse parameters (area, eccentricity, and tilt) for the pupil aperture that would produce the entrance pupil appearance observed by Wyatt (1995) at the two light levels. A hyperbolic tangent function of pupil aperture radius is used to transition between the elliptical eccentricity of the constricted pupil, through circular at an intermediate size, to the eccentricity of the dilated pupil. Consistent with Wyatt (1995), the tilt

of the elliptical pupil aperture is horizontal ($\theta = 0$) for all pupil sizes below the circular intermediate point, and then vertical with a slight tilt of the top towards the nasal field for all larger pupils.

The model therefore provides a pupil that smoothly transitions in elliptical eccentricity and horizontal-to-vertical orientation (passing through circular) as the radius of the pupil aperture varies from small to large following these functions:

$$\epsilon(r) = 0.145(4.770(tanh(r - 1.749) + 0.099))$$
$$\theta(\epsilon) = \begin{cases} 0 & \text{if } \epsilon < 0; \\ \frac{3}{7}pi & \text{if } \epsilon > 0; \end{cases} \tag{3}$$

where r is the radius of the pupil aperture in mm, ϵ is the non-linear eccentricity of the aperture ellipse, and θ is the tilt of the aperture ellipse (horizontal = 0; vertical = $pi/2$). The sign of ϵ is used to determine θ, although the absolute value of ϵ is used to generate the pupil aperture ellipse.

Although not required to determine the entrance pupil, the boundary of the visible iris is modeled for comparison with empirical images of the eye. The horizontal visible iris diamter (HVID) has been reported to be 11.8 mm (Caroline & Andre, 2002). Bernd Bruckner of the company Appenzeller Kontaktlinsen AG measured HVID using photokeratoscopy in 461 people (Brückner, n.d.) and kindly supplied me with the individual subject measurements. These data are well fit with a Gaussian distribution and yield a mean iris radius of 5.91 mm and a standard deviation of 0.28 mm. After accounting for corneal magnification, the radius of the iris in the model is set to 5.57 mm. The center of the iris circle is displaced slightly (0.35 mm) from the optical axis in the nasal and vertical direction. This accounts for the tilt and tip of the corneal ellipsoid with respect to the optical axis, thus maintaining a consistent radial distance between the edge of the visible iris border and inner surface of the cornea.

Lens

As we do not perform ray-tracing originating from the retina, the lens is modeled chiefly for completeness of the illustration. The parameters of the hyperbolas that model the front and rear surface of the lens are taken from Atchison (2006). A single nodal point is specified and used for calculation of the visual axis. This point is placed on the optical axis and 7.2 mm posterior to the corneal surface, representing the mid-point of the nodal points obtained in the Gullstrand-Emsley simplified schematic eye (Emsley, 1948).

Posterior chamber

Atchison (2006) provides the radii of curvature and asphericities of a biconic model of the posterior chamber, which is decentred and tilted with respect to the visual axis. With increasing negative refractive error (myopia), the posterior chamber changes size, elongating in the axial direction and to a lesser extent in the vertical and horizontal directions. I model the posterior chamber as an ellipsoid that is centered on and aligned with the optical axis. I converted the 4 parameters of the Atchison biconic model to 3 radius values of an ellipsoid by numeric approximation, including the change in the radii of the ellipsoid with variation in ametropia:

$$posterior_chamber_radius_{axial}(SR) = 10.1760 - 0.1495SR$$
$$posterior_chamber_radius_{horizontal}(SR) = 11.4558 - 0.0393SR \tag{4}$$
$$posterior_chamber_radius_{vertical}(SR) = 11.3771 - 0.0864SR$$

These values differ slightly from the ellipsoid radii provided by Atchison (2006) as the current model maintains the same axial length as the Atchison model but for a posterior chamber that remains aligned with the optical axis. Therefore, the total axial length of the eye along the optical axis follows the same formula as Atchison (2006):

$$axial_length(SR) = 23.58 - 0.299SR \tag{5}$$

Visual axis

Our goal is to describe the appearance of the entrance pupil. Often, the pupil is observed while the subject under study has their eye directed at a fixation point. To model this, we specify the visual axis of the eye, and its angle with respect to the optical axis. We assume that the pupillary and optical axes of the eye are aligned, following empirical work that finds the misalignment to be quite small (Atchison et al., 2014). The visual axis is defined by the line segments that connect the fovea of the eye with the fixation target through the nodal points. While not a single line, a convenient approximation is to describe the visual axis by the segment that connects the fovea to the average location of the two nodal points. The angle between the visual and optical axes of the eye is termed α.[1] A related measurement is κ, which is the angle between the pupillary and visual axes. As the optical and pupillary axes of the the current model are aligned, we will use the term α to refer to both of these values.

The visual axis is generally displaced nasally and superiorly within the visual field relative to the optical axis. The horizontal displacement of the visual axis is $5 - 6°$, but this varies with spherical refractive error, becoming smaller in myopia (Tabernero et al., 2007). Vertical displacement is on the order of $2 - 3°$ but shows greater variability and less of a dependence upon ametropia (Gharaee et al., 2015; Tscherning, 1920; Qi et al., 2016).

In the current model, the visual axis is derived by first specifying the location of the fovea in units of retinal degrees along each dimension of the posterior chamber ellipsoid, referenced to the posterior apex of the posterior chamber (which is the point at which the optical axis intersects the retina). The foveal location in the emmetropic eye is set such that the angle α in degrees of visual field is $5.8°$ nasal and $2.5°$ superior. To model the effect of refractive error upon α, the distance of the fovea from the posterior chamber apex is scaled by the relative ellipticity of the posterior chamber:

$$\begin{aligned} s(SR) &= 1 - \frac{posterior_chamber_radius_{axial}(SR)}{posterior_chamber_radius_{horizontal}(SR)} \\ FA_horizontal(SR) &= FA_horizontal_0 * \frac{s_{SR}}{s_0} \end{aligned} \tag{6}$$

where $FA_horizontal$ is the distance of the fovea from the posterior pole of the posterior chamber in degrees of ellipse, s is a scaling factor, *SR* is the spherical refractive error, and $FA_horizontal_0$, s_0 are the values for the emmetropic eye. As the posterior chamber becomes more spherical with increasing myopia, s approaches zero and the model shrinks the foveal position towards the optical axis. If the modeled eye is hyperopic, then $s > 1$ and the distance of the fovea from the point of the intersection of the optical axis grows proportionately. The scaling of foveal angle in the vertical direction is a straightforward extension that uses the vertical radius of the posterior chamber ellipse.

The visual axis for the model is then obtained by finding the angle between the optical axis and the line that connects the fovea with the mean nodal point of the eye. The change in the location of the fovea and the corresponding change in α can be seen in Figure 1 by comparing the visual axis between the emetropic and myopic eyes.

I compared the properties of this model of the visual axis to empirical data. Figure 2 presents measurements of κ as a function of cycloplegic refractive error for 279 subjects (Hashemi et al. 2010; raw data kindly provided by the corresponding author). The median κ value for emmetropic subjects (defined as having an absolute refractive error of 0.5 diopters or less) was $5.8°$, and is indicated with a plus symbol. In red is the α angle function returned by the current model for eyes with varying refractive error. In blue is an alternate model of α provided by Tabernero et al. (2007) that holds the fovea at a constant horizontal distance from the optical axis as the axial length of the eye is increased or decreased. The Tabernero model tends to under-predict α for emmetropic eyes and over-predict for myopic eyes.

[1] I adopt the axis terms and Greek letter designations of Atchison et al. (2000)

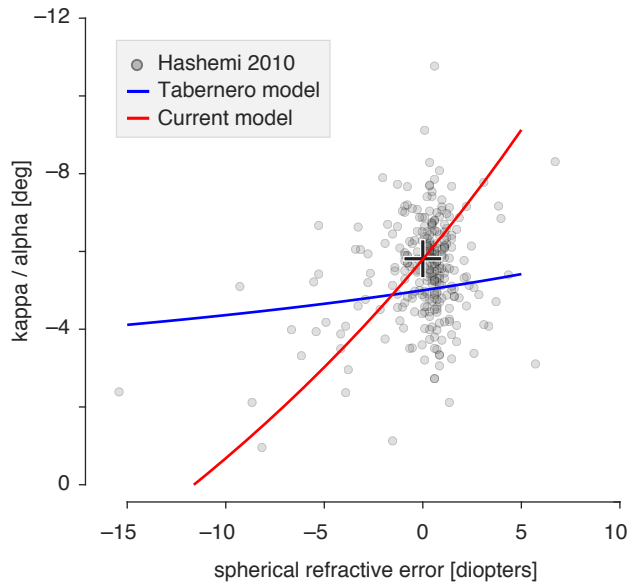

Figure 2: **Kappa by spherical refractive error** The angle between the visual axis and the pupillary axis (κ) was measured by Hashemi and colleagues (2010) for 279 subjects, and these values were related to the cycloplegic refractive error for each subject (gray points). The black plus symbol indicates the median κ value observed in emmetropic subjects. The α value produced by the current model across refractive error is shown in red. The blue line indicates the values produced by the model of Tabernero and colleagues (2007).

Perspective projection and ray-tracing

Given the model eye, our goal is to specify the appearance of the pupil in an image in terms of the parameters of an ellipse. This is accomplished by perspective projection of the eye to the sensor of a simulated camera, and then fitting an ellipse to points on the border of the pupil image. This projection requires us to specify the intrinsic properties of a camera and its position in space.

Perspective projection

A pinhole camera model is defined by an intrinsic matrix. This may be empirically measured for a particular camera using a resectioning approach (Bouguet, 2000; Zhang, 2000).[2] If provided, the projection will also model radial lens distortion (Heikkila & Silven, 1997), although the simulations performed here assume no radial distortion. The position of the camera relative to the eye is specified by a translation vector in world units, and the rotation of the camera about its optical axis (torsion). As is described below, eye rotations are defined with respect to the alignment of the optical axis of the eye with the optical axis of the camera; a consequence is that the azimuth and elevation of the camera relative to the world coordinate frame may be ignored.

With these elements in place, the model defines equally spaced points on the boundary of the front and back pupil aperture with a specified radius in millimeters. As the pupil aperture is elliptical, radius is defined in terms of a circle of equivalent area. Five boundary points uniquely specify an ellipse; six or more are required to measure the deviation of the shape of the pupil boundary from an elliptical form. The boundary points from the front and back pupil aperture are projected to the image plane. A combination of points from the front and back aperture define the entrance pupil, depending upon the angle with which the eye is viewed. The set of boundary points is identified, and then fit with an ellipse (Fitzgibbon et al., 1999), yielding the ellipse parameters.

[2]This is also termed “camera calibration” but the term “resectioning” is preferred here as it avoids confusion with spectroradiometric calibration of a device.

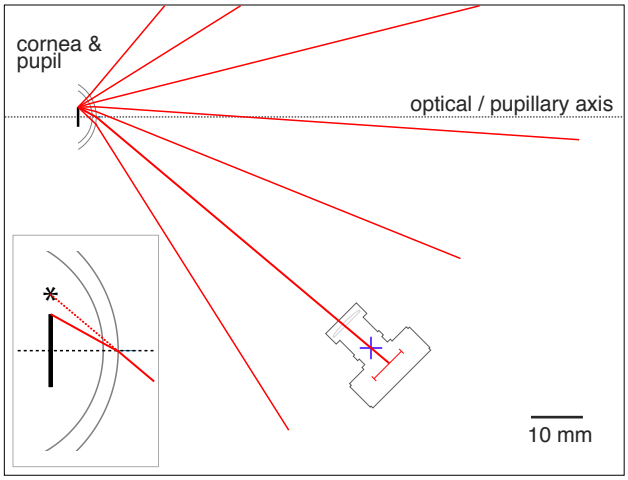

Figure 3: **Calculation of the virtual image location of a pupil boundary point** This 2D schematic shows the cornea and a 2 mm radius pupil aperture of the model eye. A camera is positioned at a $45°$ viewing angle relative to the optical axis of the eye. The optical system is composed of the aqueous humor, the back and front surfaces of the cornea, and the air. We consider the set of rays that might originate from the edge of the pupil. Each of these rays depart from the pupil aperture at some angle with respect to the optical axis of the eye. We can trace these rays through the optical system. Each ray will pass at a varying distance from the nodal point of the camera (blue +). For a pinhole camera, only the ray that strikes the nodal point exactly (i.e., at a distance of zero) will contribute to the image. We therefore search across values of initial angle to find the ray that minimizes the nodal point distance. In this example system, a ray that departs the pupil point at an angle of $-30°$ with respect to the optical axis of the eye strikes the nodal point of the camera after undergoing refraction by the cornea. *Inset bottom left.* Given the path of the ray after it exits the last surface of the optical system (in this case, the front surface of the cornea), we can project back to the plane of the pupil, and assign this as the point in the coordinate space from which the ray appeared to originate. This is the virtual image location for this pupil point.

Ray tracing

As viewed by the camera, the pupil boundary points are subject to corneal refraction, and thus are virtual images. The cornea causes the imaged pupil to appear larger than its actual size, and displaces and distorts the shape of the pupil when the eye is viewed off-axis (Barsingerhorn et al., 2017; Fedtke et al., 2010). A similar and additional effect is introduced if the eye is observed through corrective lenses worn by the subject (e.g., contacts or spectacles).

To account for these effects, the projection incorporates a ray-tracing solution. I model the cornea of the eye and any corrective lenses as ellipsoidal surfaces that are centered on the optical (and thus pupillary) axis of the eye. The set of surfaces (with their radii, position, and refractive indices) constitute the optical system. The routines provide refractive indices for the aqueous humor and cornea, as well as values for materials that are present in the optical path as artificial corrective lenses (e.g., hydrogel, polycarbonate, CR-39). The refractive indices specified by the model account for the spectral domain in which the eye appearance is being modeled (i.e., visible or near infrared), with the specific values derived from a variety of sources (Childs et al., 2016; Nikolov & Ivanov, 1999, 2000; Sardar et al., 2007; Traynor et al., 2017). The position, curvature, and thickness of any modeled corrective lenses are computed by the analysis routines, based upon the specified spherical correction of the lens in diopters.

For the specified optical system, I implement 3D tracing for skew rays through a system of ellipsoidal surfaces (Lin, 2017). Given a boundary point on the pupil aperture, and the angles with which the ray departs from the optical axis of the eye, and given values for the rotation of the eye and spatial translation of the camera, we can compute how closely the ray passes the nodal point of the camera (Figure 3). We search for the ray that exactly intersects the nodal point of the camera and thus will uniquely be present in the resulting image (assuming a pinhole aperture). Given the position and angle of this ray as it leaves the last surface in the optical system, we can project back to the apparent (virtual) point of origin of the ray in the pupil plane.

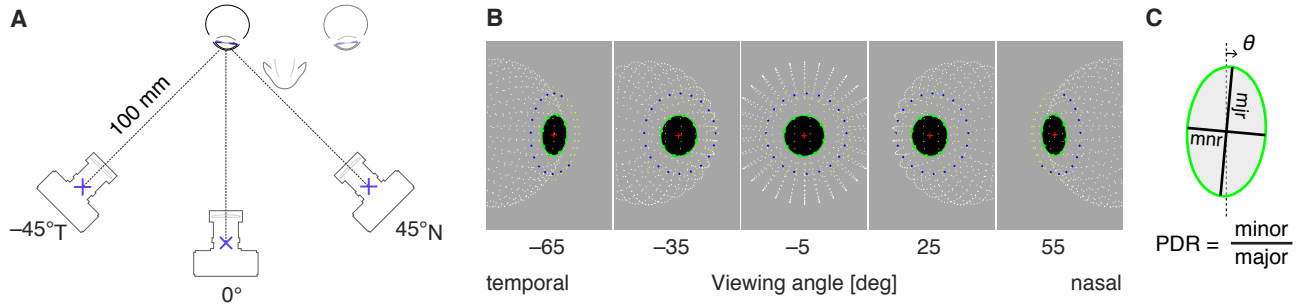

Figure 4: **Simulation of measurements of Mathur and colleagues 2013**. (A) A camera was positioned 100 mm from the cornea at different viewing angles within the temporal and nasal visual field. The visual axis of the eye was aligned with the optical axis of the camera at a viewing angle of zero. (B) The output of the current model is shown for equally spaced ($30°$) viewing angles from the temporal to nasal visual field. In the center image, viewed at $-5°$, the optical axes of the eye and camera are nearly aligned in the horizontal plane. The points shown correspond to the posterior chamber (white), visible iris border (blue), pupil border points and fitted ellipse (green), front corneal surface (yellow), and the center of the pupil aperture (red plus). The iris border and pupil border points have been subjected to refraction by the cornea. Iris border points are missing in some views as these points encountered total internal reflection during ray tracing. (C) The pupil diameter ratio (PDR) is the ratio of the minor to the major axis of an ellipse fit to the entrance pupil. θ is the tilt of the major axis of the pupil ellipse.

Entrance pupil of a stationary eye

The ellipse parameters of the entrance pupil produced by the current model may be compared to empirical measurements. Mathur et al. (2013) obtained images of the pupil of the right eye from 30 subjects. Each subject fixated a target. A camera was positioned 100 mm away from the corneal apex and was moved to viewing angle positions in the temporal and nasal visual field within the horizontal plane. A viewing angle of zero was assigned to the position at which the visual axis of the subject was aligned with the optical axis of the camera. At each angular viewing position, the camera was translated slightly to be centered on the entrance pupil. The pupil of the subject was pharmacologically dilated (and the eye rendered cycloplegic) with 1% cyclopentolate. The subjects had a range of spherical refractive errors, but the central tendency of the population was to slight myopia; I calculated the weighted mean spherical error to be –0.7 diopters. Figure 4a illustrates the geometry of the measurement.

The Mathur et al. (2013) measurements can be simulated in the current model. I created a right eye with a spherical refractive error of –0.7 diopters, and assumed an entrance pupil diameter of 6 mm to account for the effect of cyclopentolate dilation (Kyei et al., 2017) (accounting for corneal magnification, this corresponds to a 5.3 mm diameter pupil aperture). I rotated the eye so that the visual axis was aligned with the optical axis of the camera at a visual field position of zero. I then positioned the camera as described in Mathur et al. (2013). Figure 4b presents renderings of the model eye as viewed from the nasal and temporal visual field.

Pupil diameter ratio

At each viewing angle Mathur et al. (2013) measured the ratio of the minor to the major axis of the entrance pupil, termed the pupil diameter ratio (PDR; Figure 4c). These measurements were combined across subjects and accurately fit by a parameterized cosine function. Figure 5a shows the resulting fit to the empirical data. The PDR decreases as a function of viewing angle, as the entrance pupil is tilted away from the camera and the horizontal axis is foreshortened. As Mathur et al. (2013) describe, the observed entrance pupil follows a cosine function that is "both decentered by a few degrees and flatter by about 12% than the cosine of the viewing angle."

Using the current model, I calculated the PDR for the entrance pupil with the camera positioned at a range of viewing angles. The model output (Figure 5b; red dashed line) agrees well with the empirical measurements. I restricted the model evaluation to viewing angles between $-65°$ and $55°$ as, beyond these angles, an ellipse provides an increasingly imperfect fit to the entrance pupil boundary (see below).

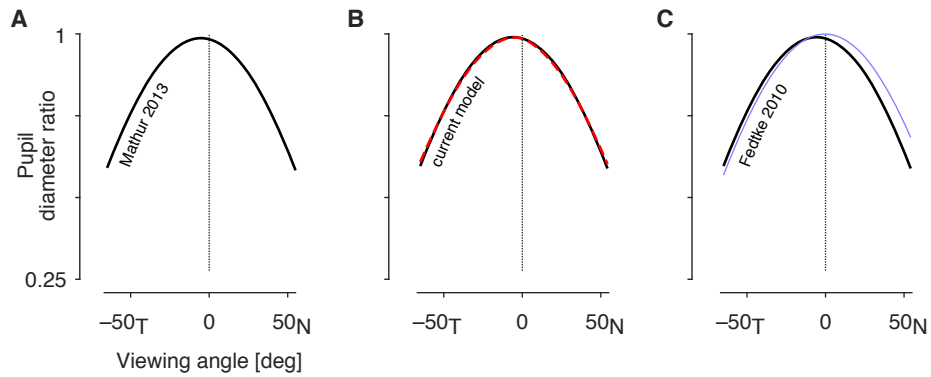

Figure 5: **Empirical and modeled pupil diameter ratios**. (a) The PDR as a function of viewing angle that was observed by Mathur and colleagues in 30 subjects. Note that the peak PDR is slightly less than one, indicating that the pupil always had an elliptical shape with a vertical major axis in these measurements. Also, the peak value is shifted away from a viewing angle of zero. (b) The current model provides the parameters of the entrance pupil ellipse. When the experimental conditions of Mathur and colleagues are simulated in the model, the resulting PDR function (dashed red line) agrees well with the empirical result. (c) In blue is the output of a model of the entrance pupil presented by Fedtke and colleagues in 2010.

Fedtke et al. (2010) examined the properties of a simulated entrance pupil, assuming a rotationally symmetric model eye with an iris of zero thickness, a circular pupil aperture, and in which the visual and optical axes were aligned. The PDR of their model as a function of viewing angle is plotted in blue in Figure 5c.

We may examine how components of the current model contribute to the replication of the empirical result. The simulation was repeated with successive addition of model components. The simplest model assumes a circular pupil aperture in an iris of zero thickness, no corneal refraction, and alignment of the pupillary and visual axes of the eye. Under these circumstances the entrance pupil behaves exactly as a function of the cosine of the viewing angle (Figure 6a). Next, we rotate the eye so that the visual axis is aligned with the optical axis of the camera when the viewing angle is zero (Figure 6b). Modeling of α (the misalignment of the visual and optical axes) decenters the PDR function. Addition of refraction by the cornea (Figure 6c) flattens the PDR function, as the entrance pupil now demonstrates magnification along the horizontal axis with greater viewing angles. Notably, however, the modeled PDR is greater than empirical observations. Modeling the thickness of the iris (Figure 6d) corrects for this by reducing the width of the entrance pupil at larger viewing angles. This is because the entrance pupil is now bounded by a combination of the back and front pupil apertures (Jay, 1962). Finally, the model is augmented with an elliptical pupil aperture (Figure 6e). Because the dilated pupil aperture is itself taller than it is wide, the PDR function is reduced overall, bringing the model into final alignment with the empirical result.

Variation in the pupil diameter ratio function

Mathur et al. (2013) found that the empirical PDR function could be fit with great accuracy by the expression:

$$PDR(\phi) = Dcos\left[\frac{\phi - \beta}{E}\right] \tag{7}$$

where ϕ is the viewing angle in degrees, D is the peak PDR, β is the viewing angle at which the peak PDR is observed (e.g., the "turning point" of the function), and $180E$ is the half-period of the fit in degrees. When fit to the output of the current model, we recover the parameters $D = 0.98$, $\beta = -5.30$, and $E = 1.14$, which are quite close to the parameters found by Mathur et al. (2013) (0.99, –5.30, and 1.12) in the fit to empirical data.

We may consider how biometric variation in the model changes the observed entrance pupil in terms of these parameters. The value D reflects almost entirely the eccentricity and tilt of the pupil aperture ellipse (Eq. 3), with an additional, small effect of the vertical component of α. Wyatt (1995) found individual variation in pupil shape. While this variation in pupil aperture ellipticity will produce variations in D, overall this model component had a rather small effect upon the simulated PDR (Figure 6).

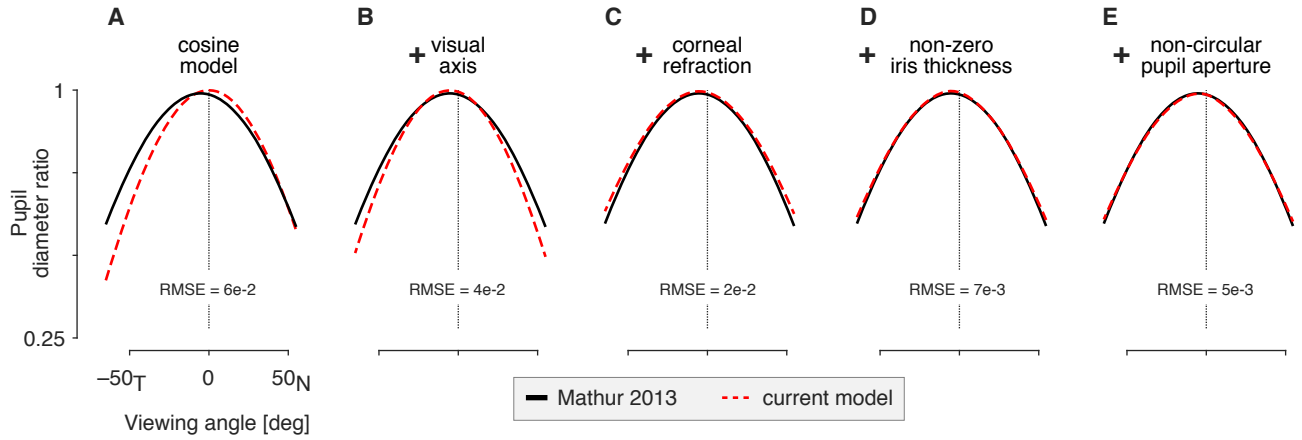

Figure 6: **Effect of model components upon the entrance pupil diameter ratio function**. In black is the Mathur and colleagues (2013) empirical result. The dashed red line is the behavior of the current model with the successive addition of model components (a-e). The root mean squared error (RMSE) between the model and the Mathur empirical result is given in each panel.

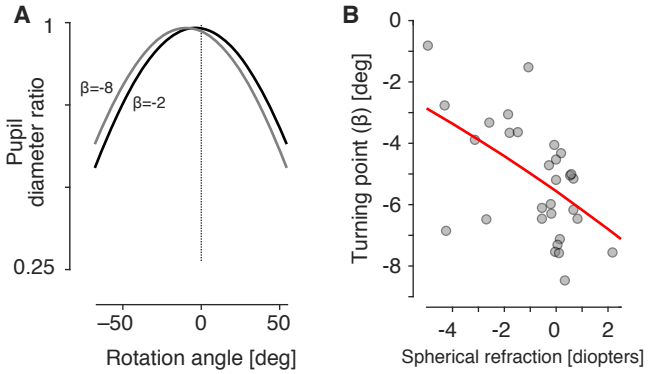

Figure 7: **Variation in turning point**. (A) The pupil diameter ratio was calculated using Equation 7 using $D = 0.98$, $E = 1.14$, and β values of -8 and -2. (B) In each of 30 subjects, Mathur and colleagues (2013) measured the viewing angle at which the peak pupil diameter ratio was observed (β), and related that value to the spherical refractive error of the subject. These data points (gray) are shown, along with turning point values returned by the current model when supplied with an eye of varying refractive error (red line). The model function is not linear, but is well approximated by the line $-5.76 - 0.59SR$, which is similar to the linear fit to the data points, which is $-5.73 - 0.61SR$.

The value β is determined by the horizontal component of α, which can vary substantially by subject and is related to spherical refractive error. Figure 7A illustrates the PDR function associated with two different β values. Mathur et al. (2013) obtained β for each of their 30 subjects and related this to subject variation in spherical refractive error. Figure 7B replots their data (gray points). The red line is the output of the current model, evaluated with simulated eyes of different spherical refractive errors. The model behavior is very close to the linear fit to the turning point data of Mathur et al. (2013). This indicates that the current model accurately captures the change in α—and thus the change in the behavior of the entrance pupil—that accompanies varying spherical refractive error.

The value E varies the "width" of the PDR function (Figure 8A). In their simulation, Fedtke et al. (2010) found that decreasing the modeled pupil aperture narrowed the PDR function (i.e., the parameter E decreased). I examined the behavior of the current model with changes in several biometric components (Figure 8B). Changes in pupil diameter had the largest effect upon the shape of the entrance pupil, followed by changes in the thickness of the iris. The depth of the iris relative to the corneal surface had a minimal effect, suggesting that changes in accommodation (apart from a change in pupil size) will have little effect upon the shape of the entrance pupil. I examined as well the effect of variation in corneal curvature. Because the cornea is modeled as a tri-axial ellipsoid, an observer that

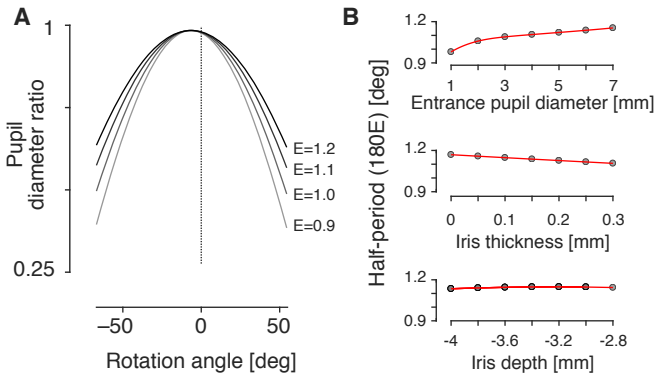

Figure 8: **Variation in half-period width**. (A) The pupil diameter ratio was calculated using Equation 7 using $D = 0.98$, $\beta = -5.30$, and E values ranging from 0.9 to 1.2. (B) The simulation was conducted with variation in pupil size (*top*), iris thickness (*middle*), and iris depth (*bottom*) and variation in the E parameter assessed. Cubic-spline fits to the points are shown in red.

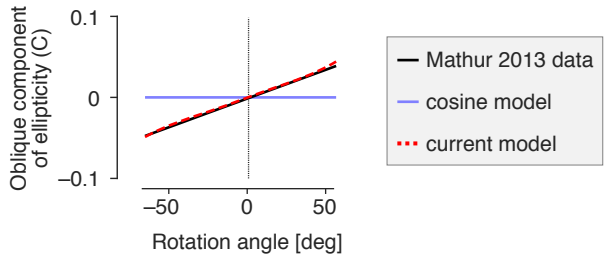

Figure 9: **Oblique component of pupil ellipticity**. The tilt of the pupil ellipse varies with viewing angle. Mathur and colleagues (2013) measured component "C" of the pupil ellipse, which was calculated as $(1 - PDR)sin[2(\theta - \frac{\pi}{2})]$, where θ is the tilt of the entrance pupil ellipse. Their observed C values are plotted in black. A simple cosine model of a circular entrance pupil (blue) does not have any ellipse tilt. The current model (dashed red line) replicates the Mathur empirical result well (RMSE = 2e-3).

moves across horizontal viewing angles encounters a different profile of corneal curvature than does an observer moving across vertical viewing angles. The current model returns an E value of 1.14 for variation in horizontal viewing angle, and a value of 1.19 across vertical viewing angle. This finding indicates that the precise values of corneal curvature have a small, but not negligible, influence upon pupil appearance.

Tilt of the entrance pupil ellipse

Mathur et al. (2013) measured the "oblique component of pupil ellipticity" (termed component "C"), which reflects the tilt of the major axis of the pupil ellipse away from vertical. I calculated this component for the current model and found that the result compares quite well with the empirical measurements (Figure 9). This tilt component of the entrance pupil ellipse can be appreciated in the rendered eye depictions (Fig 4b), with the top of the pupil tilted towards the nasal field when the eye is viewed from the temporal field, and vice-a-versa. This tilt is almost entirely the result of modeling the vertical displacement of the visual axis from the optical axis; there is a small additional effect of the tilt of the dilated pupil aperture ellipse.

Error in ellipse fitting to entrance pupil boundary

Finally, I examined how well the entrance pupil is described by an ellipse as a function of viewing angle by calculating the root mean squared distance of the entrance pupil border points from the fitted ellipse (Figure 10). Overall, the ellipse fit error is small relative to the 6 mm diameter of the entrance pupil, although this error grows systematically as a function of viewing angle. The particular form of the error function close to zero viewing angle is the result of the transition point at which the back pupil aperture first begins to

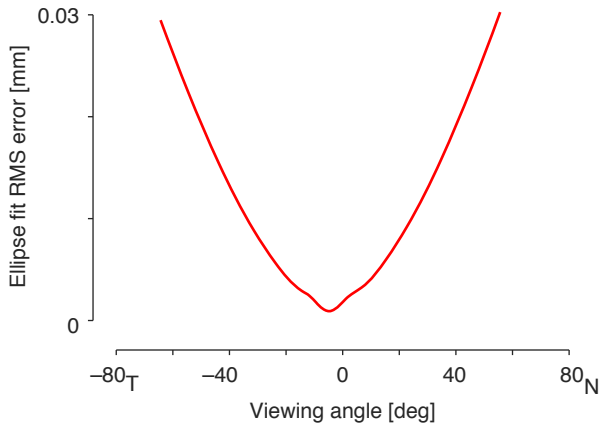

Figure 10: **Ellipse fit error**. The set of points that define the pupil boundary in the image are not exactly elliptical, due to the refractive effects of the cornea and the joint influence of the back and front pupil aperture on the resulting entrance pupil. The root mean squared distance of the pupil boundary points from the best fitting ellipse as a function of viewing angle is shown. The fitting error is expressed in mm.

influence the entrance pupil boundary.

Entrance pupil of a rotating eye

A potential application of the current model is to fit the appearance of the entrance pupil as seen by a stationary camera while the eye undergoes occulomotor rotation. This fit may be used to derive the rotation of the eye and the size of the pupil, and thus provide model-based eye tracking. To support this application, the model is augmented with the ability to pose the eye at different rotational angles. Figure 11 shows the schematic eye after undergoing a 30° azimuth or elevation rotation, and how the consequence of this rotation differs by eye size.

Rotation centers

I specify rotations of azimuth, elevation, and torsion in terms of an extrinsic, head-fixed coordinate frame. Within this frame, Listing's Law corresponds to holding torsion constant across rotations of azimuth and elevation. For the simulations described below, I adopt the convention that an eye rotation of zero corresponds to an alignment of the visual and optical axis.[3]

The eye rotates about a point located within the globe. The rotation center of the eye is often treated as a single, fixed point. A typical assumption is that the eye center of rotation in emmetropes is 13.3 mm behind the corneal apex (Von Noorden & Campos, 2002). This value appears to be a compromise between the different centers of rotation that are obtained for azimuth and elevation eye rotations. Fry and Hill in 1962 and 1963 reported that the center of azimuth rotation is on average 14.8 mm posterior to the corneal apex and displaced slightly nasal to the visual axis of the eye. The center for elevation rotation is not as deep, being 12.2 mm posterior to the corneal apex and displaced slightly superiorly to the visual axis.[4] This difference in the effective center of eye rotation for horizontal and vertical eye movements was subsequently observed by Hayami and colleagues (2002). Fry and Hill found that only a small subset of subjects (2 of 31) had translation of the eye with rotation. Earlier measurements by Park and Park (1933) had claimed substantial translation of the eye during rotation as a feature of all subjects, although this result was attributed by Fry and Hill to an incorrect assumption that all "sight lines" (i.e., rotations of the visual axis of the eye) pass through the same point in space. We therefore model a fixed point of eye rotation, although adopt separate centers for azimuth, elevation, and torsion movements (the torsion rotation center

[3]This convention is to facilitate comparison of the rotated eye results to the stationary eye results that were reported earlier as as function of viewing angle relative to the visual axis. The actual model assigns a zero azimuth and elevation to the pose of the eye that aligns to the optical axes of the eye and camera.

[4]While the current model is in optical axis coordinates, the effect of this difference is very small (less than 1/100th of a millimeter) so it is ignored.

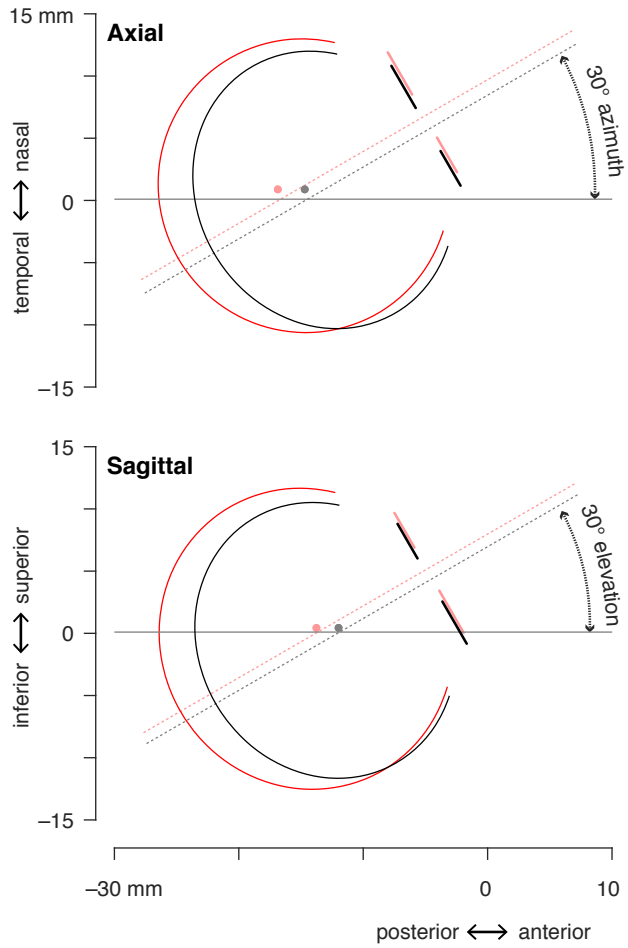

Figure 11: **Schematic of the rotated model eye** The posterior chamber, iris, rotation center, and optic axis are shown for an emmetropic (gray) and myopic (red; –10 diopter) model eye. (*Top*) In the axial view, the centers for azimuthal rotation are shown (filled circles). Myopia increases axial length and displaces the rotation center posteriorly. The eyes have undergone a 30° rotation in azimuth. The original optical axis is shown as a solid line, and the rotated optical axis is dashed. Note that the position of the pupil aperture after a given eye rotation differs by the axial length of the eye. (*Bottom*) In the sagittal view, the centers for rotation in elevation are shown (filled circles). Note that the rotation center for elevation lies anterior to the rotation center for azimuth.

being on the optic axis). A small, transient retraction and torsion of the eye has been demonstrated to occur following a saccade (Enright, 1986); we do not attempt to model this.

Spherical ametropia is correlated with the axial length of the eye. We assume here that the center of rotation reflects this change in length. Fry and Hill found that depth of the center for rotation in azimuth increased by 0.167 mm for each negative diopter of spherical refraction, and elevation rotation depth by 0.15 mm for each negative diopter. Dick and colleagues (1990) found that for each mm of increase in axial length, the center of rotation increased in depth by 0.5 mm. Given that in Atchison et al. (2005) the axial length of the eye was found to increase by 0.299 mm for each negative diopter of spherical ametropic error, this would imply a lengthening of the radius of eye rotation by 0.15 mm, which is in good agreement with the Fry and Hill observation of 0.15 - 0.167 mm of increase. We therefore scale the azimuth and elevation rotation centers by the ratio of the specified posterior chamber radii relative to the emmetropic size of this structure. The shift of the rotation centers to a greater depth relative to the corneal surface with myopia can be seen in Figure 11.

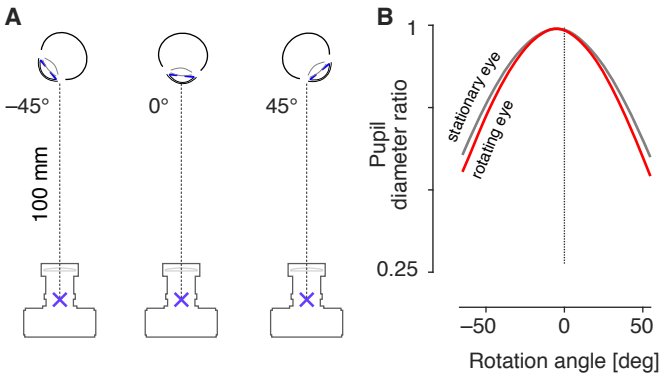

Figure 12: **Pupil appearance in a rotating eye**. (A) A simulated camera was positioned 100 mm from the anterior surface of the cornea, centered on the entrance pupil when the eye was at a rotation angle of zero degrees. (B) In red is the pupil diameter ratio as a function of the rotation of the eye. For comparison, the PDR as a function of viewing angle for a stationary eye is shown in gray. When observed as the eye rotates, the PDR function is narrower ($E = 1.06$) as compared to when the camera orbits the stationary eye ($E = 1.14$).

Pupil diameter ratio of a rotating eye

The current model was evaluated with an eye with a –0.7 refractive error, positioned at a fixed location 100 mm from the camera. I obtained the PDR for the entrance pupil as the eye rotated through azimuth (Figure 12A). The PDR function for the entrance pupil is narrowed (i.e., the E parameter of Eq 7 is lower) as compared to that obtained when the camera is orbited around the eye (Figure 12B). This is because the rotation of the plane of the pupil away from the camera in depth induces further foreshortening of the entrance pupil ellipse.

The refractive error of the eye has essentially no effect upon the E parameter of the PDR function when the eye is stationary. I examined if this is also the case for the rotating eye, as variation in spherical ametropia alters the depth of the rotation center of the eye, and thus could modify the degree of pupil ellipse foreshortening with rotation. When the simulation was repeated assuming eyes with a range of spherical refractive error, however, the effect of eye length upon this aspect of pupil appearance was minimal. Assuming a refractive error ranging from –10 to +5 diopters caused E to vary only from 1.05 to 1.06.

Discussion

I find that an "exact" model eye is able to reproduce empirical measurements of the shape of the entrance pupil with good accuracy. More generally, the current study provides a "forward model" of the appearance of the pupil as observed by a camera at an arbitrary position, and with the eye undergoing biologically accurate rotation.

Similar to the current study, Fedtke et al. (2010) had the goal of using a ray-traced model eye to examine the properties of the entrance pupil as compared to empirical measures. The current study builds upon Fedtke et al. (2010) in several respects. First, the anatomical accuracy of the anterior chamber of the model eye is advanced, incorporating iris thickness, an elliptical pupil aperture, and a tri-axial cornea. These refinements both improve the match to empirical observations (Mathur et al., 2013) and support the generalization of the model to arbitrary pupil sizes, and to viewing angles apart from the horizontal plane.

The current model also accounts for the effect of refractive error upon the angle α between the visual and optical axes. The model assigns a location for the fovea on the retina, the position of which is moved across the retinal surface by the relative sphericity of the posterior chamber. While in good agreement with empirical measurements of the visual axis (Hashemi et al., 2010; Mathur et al., 2013), the modeled behavior of the foveal location is not easily related to one of the mechanisms of axial lengthening considered in myopia (Verkicharla et al., 2012). Atchison (2006) described a model of spherical ametropia in which the posterior chamber is progressively decentered from the visual axis with greater negative refractive error. The current model (which is organized with respect to the optical

axis) could capture this behavior, and perhaps the movement of the fovea, by rotating the posterior chamber as a function of spherical refractive error. I regard this as a topic for future investigation as part of an effort to model the position of retinal landmarks (i.e., the fovea, optic disc, and optical axis intersection) as a function of ametropia.

The current model also supports biologically accurate eye rotation. There is an extensive literature in which anatomically-inspired models of the eye are used to inform gaze and pupil tracking systems (e.g., Barsingerhorn et al., 2017; Böhme et al., 2008). These applications have a particular focus upon determining the location of the first Purkinje image and the center of the entrance pupil, as these may be used deduce gaze angle. While not studied here, these values could be derived readily from the current model. The effect of biometric variation upon these values may also be examined. For example, while variation in refractive error had little effect upon the width of the PDR function (value E) across eye rotation, the position of the center of the entrance pupil as a function of eye rotation will be strongly influenced by spherical ametropia and the resulting shift in the rotation centers of the eye.

For eye tracking applications, a relevant feature of the current model is that it is implemented in custom made, open-source MATLAB code, as opposed to within general optical bench software (e.g., Zemax). The ray-tracing operations of the model are conducted using compiled functions. As a result, the routines execute quickly and can form the basis for an "inverse model" that searches across values of eye rotation and pupil radius to best fit an observed eye tracking image.

The biometric parameters that define the model were set by reference to prior empirical measurements. In an effort to best fit the pupil diameter ratio function of Mathur et al. (2013), three model parameters were tuned "by hand": the maximum, dilated entrance pupil ellipticity was held to a value slightly smaller than that reported by Wyatt (1995); iris thickness at the pupil aperture was set to 0.15 mm; and the value for vertical α was set to $2.5°$ in the emmetropic eye. Because these parameter values are biologically plausible and within the range of prior empirical measurements, I am optimistic that the model will generalize well to novel observations of entrance pupil appearance. The values for the rotation centers of the eye were derived from two classic studies (G. Fry & Hill, 1962; G. A. Fry & Hill, 1963), and I am unaware of more recent work that constrains the location and possible separation of the azimuth and elevation centers of the eye (with the exception of Hayami et al., 2002). The accuracy of the particular values for eye rotation used here would ideally be confirmed against observations of the entrance pupil in eyes with different refractive errors, perhaps undergoing calibrated rotations in azimuth and elevation.

References

Atchison, D. A. (2006). Optical models for human myopic eyes. *Vision research*, *46*(14), 2236–2250.

Atchison, D. A., Mathur, A., Suheimat, M., & Charman, W. N. (2014). Visual field coordinates of pupillary circular axis and optical axis. *Optometry and Vision Science*, *91*(5), 582–587.

Atchison, D. A., Pritchard, N., Schmid, K. L., Scott, D. H., Jones, C. E., & Pope, J. M. (2005). Shape of the retinal surface in emmetropia and myopia. *Investigative Ophthalmology & Visual Science*, *46*(8), 2698–2707.

Atchison, D. A., Smith, G., & Smith, G. (2000). Optics of the human eye.

Barsingerhorn, A., Boonstra, F., & Goossens, H. (2017). Optics of the human cornea influence the accuracy of stereo eye-tracking methods: a simulation study. *Biomedical optics express*, *8*(2), 712–725.

Böhme, M., Dorr, M., Graw, M., Martinetz, T., & Barth, E. (2008). A software framework for simulating eye trackers. In *Proceedings of the 2008 symposium on eye tracking research & applications* (pp. 251–258).

Bouguet, J.-Y. (2000). *Matlab camera calibration toolbox.* Available from https://www.mathworks.com/help/vision/ref/cameramatrix.html

Bradly, A., & Thibos, L. N. (1995). Modeling off-axis vision i: the optical effects of decentering visual targets or the eye's entrance pupil. In *Vision models for target detection and recognition: In memory of arthur menendez* (pp. 313–337). World Scientific.

Brückner, B. (n.d.). *HVID & SimK study* (Tech. Rep.). Appenzeller Kontaktlinsen AG.

Caroline, P., & Andre, M. (2002). The effect of corneal diameter on soft lens fitting, part 2. *Contact Lens Spectrum*, *17*(5), 56–56.

Childs, A., Li, H., Lewittes, D. M., Dong, B., Liu, W., Shu, X., et al. (2016). Fabricating customized hydrogel contact lens. *Scientific reports*, *6*, 34905.

Dick, G. L., Smith, B. T., & Spanos, P. L. (1990). Axial length and radius of rotation of the eye. *Clinical and Experimental Optometry*, *73*(2), 43–50.

Drexler, W., Baumgartner, A., Findl, O., Hitzenberger, C. K., Sattmann, H., & Fercher, A. F. (1997). Submicrometer precision biometry of the anterior segment of the human eye. *Investigative Ophthalmology & Visual Science*, *38*(7), 1304–1313.

Emsley, H. H. (1948). *Visual optics*. Hatton Press.

Enright, J. (1986). The aftermath of horizontal saccades: saccadic retraction and cyclotorsion. *Vision research*, *26*(11), 1807–1814.

Fedtke, C., Manns, F., & Ho, A. (2010). The entrance pupil of the human eye: a three-dimensional model as a function of viewing angle. *Optics express*, *18*(21), 22364–22376.

Fitzgibbon, A., Pilu, M., & Fisher, R. B. (1999). Direct least square fitting of ellipses. *IEEE Transactions on pattern analysis and machine intelligence*, *21*(5), 476–480.

Fry, G., & Hill, W. (1962). The center of rotation of the eye. *Optometry and Vision Science*, *39*(11), 581–595.

Fry, G. A., & Hill, W. (1963). The mechanics of elevating the eye. *Optometry and Vision Science*, *40*(12), 707–716.

Gharaee, H., Shafiee, M., Hoseini, R., Abrishami, M., Abrishami, Y., & Abrishami, M. (2015). Angle kappa measurements: normal values in healthy Iranian population obtained with the Orbscan II. *Iranian Red Crescent Medical Journal*, *17*(1).

Hashemi, H., KhabazKhoob, M., Yazdani, K., Mehravaran, S., Jafarzadehpur, E., & Fotouhi, A. (2010). Distribution of angle kappa measurements with orbscan ii in a population-based survey. *Journal of Refractive Surgery*, *26*(12), 966–971.

Hayami, T., Shidoji, K., & Matsunaga, K. (2002). An ellipsoidal trajectory model for measuring the line of sight. *Vision research*, *42*(19), 2287–2293.

He, M., Wang, D., Console, J. W., Zhang, J., Zheng, Y., & Huang, W. (2009). Distribution and heritability of iris thickness and pupil size in chinese: the guangzhou twin eye study. *Investigative ophthalmology & visual science*, *50*(4), 1593–1597.

Heikkila, J., & Silven, O. (1997). A four-step camera calibration procedure with implicit image correction. In *Computer vision and pattern recognition, 1997. proceedings., 1997 ieee computer society conference on* (pp. 1106–1112).

Jay, B. (1962). The effective pupillary area at varying perimetric angles. *Vision Research*, *1*(5-6), 418–424.

Kyei, S., Nketsiah, A. A., Asiedu, K., Awuah, A., & Owusu-Ansah, A. (2017). Onset and duration of cycloplegic action of 1% cyclopentolate–1% tropicamide combination. *African health sciences*, *17*(3), 923–932.

Lin, P. D. (2017). Skew-ray tracing of geometrical optics. In *Advanced geometrical optics* (pp. 29–69). Springer.

Mathur, A., Gehrmann, J., & Atchison, D. A. (2013). Pupil shape as viewed along the horizontal visual field. *Journal of vision*, *13*(6), 3–3.

Navarro, R., González, L., & Hernández, J. L. (2006). Optics of the average normal cornea from general and canonical representations of its surface topography. *JOSA A*, *23*(2), 219–232.

Navarro, R., Santamaria, J., & Bescós, J. (1985). Accommodation-dependent model of the human eye with aspherics. *JOSA A*, *2*(8), 1273–1280.

Nikolov, I. D., & Ivanov, C. D. (1999). Optical plastic refractive index measurements for nir region. In *18th congress of the international commission for optics* (Vol. 3749, pp. 554–556).

Nikolov, I. D., & Ivanov, C. D. (2000). Optical plastic refractive measurements in the visible and the near-infrared regions. *Applied Optics*, *39*(13), 2067–2070.

Park, R. S., & Park, G. E. (1933). The center of ocular rotation in the horizontal plane. *American Journal of Physiology-Legacy Content*, *104*(3), 545–552.

Qi, H., Jiang, J.-J., Jiang, Y.-M., Wang, L.-Q., & Huang, Y.-F. (2016). Kappa angles in different positions in patients with myopia during lasik. *International journal of ophthalmology*, *9*(4), 585.

Sardar, D. K., Swanland, G.-Y., Yow, R. M., Thomas, R. J., & Tsin, A. T. (2007). Optical properties of ocular tissues in the near infrared region. *Lasers in medical science*, *22*(1), 46–52.

Spring, K., & Stiles, W. (1948). Apparent shape and size of the pupil viewed obliquely. *The British journal of ophthalmology*, *32*(6), 347.

Tabernero, J., Benito, A., Alcón, E., & Artal, P. (2007). Mechanism of compensation of aberrations in the human eye. *JOSA A*, *24*(10), 3274–3283.

Traynor, N. B., McLauchlin, C., Dodge, K., McGarrah, J. E., Padalino, S. J., McCluskey, M., et al. (2017). Cr-39 (padc) reflection and transmission of light in the ultraviolet–near-infrared (uv–nir) range. *Applied spectroscopy*, 0003702817745071.

Tscherning, M. H. E. (1920). *Physiologic optics: Dioptrics of the eye, functions of the retina ocular movements and binocular vision*. Keystone Publishing Company.

Uozato, H., & Guyton, D. L. (1987). Centering corneal surgical procedures. *American journal of ophthalmology*, *103*(3 Pt 1), 264–275.

Verkicharla, P. K., Mathur, A., Mallen, E. A., Pope, J. M., & Atchison, D. A. (2012). Eye shape and retinal shape, and their relation to peripheral refraction. *Ophthalmic and Physiological Optics*, *32*(3), 184–199.

Von Noorden, G., & Campos, E. (2002). *Binocular vision and ocular motility: Theory and management of strabismus*. Mosby. Available from https://books.google.com/books?id=m6hsAAAAMAAJ

Wyatt, H. J. (1995). The form of the human pupil. *Vision Research*, *35*(14), 2021–2036.

Zhang, Z. (2000). A flexible new technique for camera calibration. *IEEE Transactions on pattern analysis and machine intelligence*, *22*(11), 1330–1334.